Wang, H., Soria Verdugo, A., Sun, J., Wang, J., Yang, Y. & Hernández Jiménez, F. (2020). Experimental study of bubble dynamics and flow transition recognition in a fluidized bed with wet particles. *Chemical Engineering Science, 211*, 115257.

DOI: 10.1016/j.ces.2019.115257

Experimental study of bubble dynamics and flow transition recognition in a fluidized bed with wet particles

Abstract: Fluidized beds containing wet granules have a wide range of applications in various industry processes. This paper studies the bubble dynamics and flow transition behavior in wet particle systems. The non-coherent algorithm was used to quantitatively calculate the bubble diameters in a three-dimensional fluidized bed system loaded with wet particles, obtaining the bubble dynamics under the action of liquid. The results indicate that the incoherent analysis can detect the formation of even tiny bubbles in the fluidized bed. The kurtosis and skewness of the pressure fluctuation signal was used to obtain the critical transition conditions of the flow pattern from turbulent to laminar. At the same time, through the decay index of the incoherent spectrum, the operating conditions of the Levy-Kolmogorov flow pattern to the Kolmogorov flow region were determined. From the comparison of the liquid bridge and the drag forces, the competitive mechanism of different forces acting on the particles that conformed the bed was analyzed, reflecting the change of the apparent minimum fluidization velocity of wet particles.

Key words: Incoherent analysis; Wet particle; Flow transition; Bubble dynamics; Turbulence

1. Introduction

Gas-solid fluidized bed reactors containing granular material with wet surfaces, can be found in various industrial processes because of its high heat transfer efficiency and mixing ability. These processes include polymerization (Zhou et al., 2013a), granulation (Poutiainen et al., 2012) , fluid catalytic cracking (FCC) reaction (Gao et al., 2001), among others. The liquid content existing in gas-solid fluidized bed can come from different sources, such as the residual contact of the previous operating unit, condensing agent, or reactants. The mixing characteristics of solids and the drying kinetics are crucial factors for the estimation of the performance of fluidized bed dryers (Wang et al., 2007). Moreover, wet particle dynamics also influences the possible subsequent processes such as combustion or gasification (Eliaers and De Wilde, 2013). For example, in the FCC process, the high-speed oil introduced is mixed with the catalyst particles and heavy hydrocarbons

are decomposed into olefinic gases, gasoline, diesel, etc. (Chen et al., 2016).

Liquid feed mode in the liquid containing fluidized bed can be classified into three main categories: spray or injection, bottom co-feed with gas phase, and premixing with dry materials. There are both experimental and numerical works available in the literature to study wet particles hydrodynamics. Bacelos et al. (2007) applied glycerol as wet medium and concluded that the concentration of glycerol had no effect on the minimum spout velocity in mono-dispersed particle system. Zhou et al. (2016a) and Bouffard et al. (2012) found that the liquid bridge force and the cohesive force changed fluidization properties of particles from Geldart B to Geldart C classification. Razzak (2018; 2007) and Zhu et al. (2000) studied the instability and flow transition characteristics of a circulating fluidized bed with liquid injections and found that two kinds of flow regimes existed and the presence of liquid changed the phase holdup. Zhou et al. (2016a; 2016b) observed stable gas-liquid-solid (G-L-S) and gas-solid (G-S) regions in a fluidized bed with continuous side-wall liquid spray, where heat transfer was enhanced by small amounts of liquid. They applied the multi-scale analysis and found that particle collision, particle circulation pattern and agglomeration behavior were dominated by the liquid cohesive force instead of the liquid evaporation with the increasing liquid feed rate.

Zhou et al. (2013a; 2013b) modelled the polymerization process with condensation of liquid and found that the bubble diameter and particle motion were hindered in the liquid-containing fluidized bed. Wang et al. (2016) applied a CFD-DEM model coupled with a liquid bridge force to study wet particle dynamics, concluding that particle velocity profiles agreed well with PIV measurement in a 2D fluidized bed. Xu et al. (2017) proposed a cohesive force model and predicted the spout behaviors of cohesive and wet particles.

From the literature reviewed, it can be inferred that wet particle dynamics affects the bubble behaviors, the flow patterns, and the agglomeration behavior significantly. The pseudo-stable fluidization state is established after the liquid is mixed. During the injection of the liquid into fluidized bed reactors, both the liquid spray position, configuration, and particle properties affect the local distribution of liquid and, thus,

result in variations of the particle fluctuation and bubble properties. In addition, liquid processing or loading ability of particles is relevant for the safe operation of the reactor and the operating conditions optimizatiom. Furthermore, as bubble dynamics are essential for the prediction of the flow pattern, mixing behavior and heat transfer in the reactors, the study of the resultant changes of bubble behavior under the effect of liquid presence in the bed is certainly important.

In this work, the flow behaviors and wet particle fluid-dynamics, considering various liquid volume fractions, are investigated by means of the incoherent analysis and time-domain analysis in a 3D fluidized bed. Firstly, the critical transition of flow pattern is recognized from the kurtosis and skewness. Then, bubble diameters are quantitatively characterized by the incoherent algorithm, obtaining both the coherent and incoherent power spectra. The decay index calculated from the dissipation region of the incoherent power indicates the change of the flow behavior from turbulent to laminar flow for higher liquid volume fractions. Furthermore, the competitive mechanism of liquid bridge and drag forces is discussed. Finally, the agglomeration behavior of wet particles is predicted by the attractor chaotic analysis for further explanation of the transition of flow behavior combined with continuous wavelet analysis.

2 Experimental setups

Experimental Apparatus. The experiments were carried out in a lab-scale cylindrical fluidized bed with an inner diameter of 8.7 cm and a height of 50 cm as shown in Fig.1. The cylindrical fluidized bed was loaded with silica sand particles of 500 μm diameter and 2500 kg/m^3 density, classified as Geldart B particles. The static bed height was set to 8.7 cm. The minimum fluidization velocity, 0.21 m/s, was measured from the standard deviation of the original pressure signals. A perforated plate gas distributor was constructed and covered with a metal mesh to distribute gas uniformly. The air flow was measured by a mass flowmeter with a range of 0-500 l/m^3 and the fluidizing air was humidified using a water column to prevent electrostatic effects. Two sets of humidity-temperature integrated sensors were located at the gas inlet and outlet of the fluidized bed to monitor the humidity change of air from the inlet to the exit.

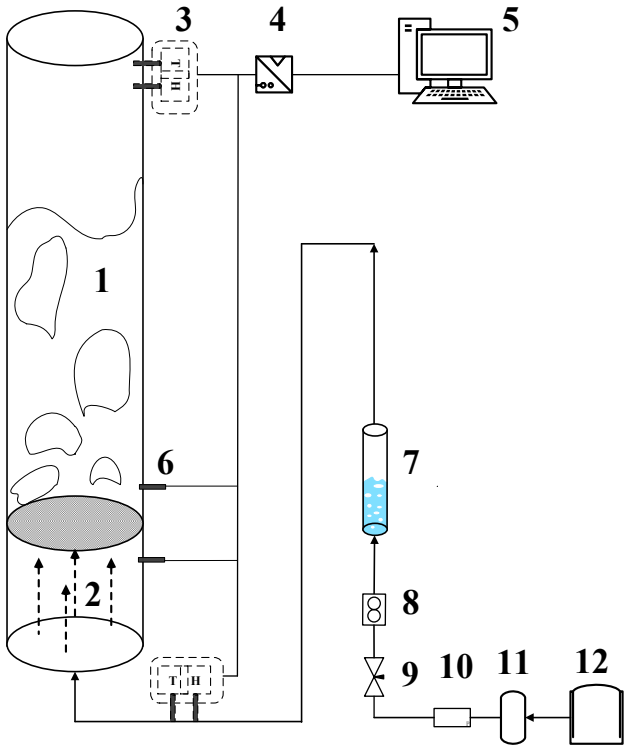

Fig.1. The experimental set-up.

1. Fluidized bed 2. Plume chamber 3. Humidity-temperature sensors 4. Data acquisition card 5. Computer 6. Kistler pressure sensors 7. Humidifier 8. Flowmeter 9. Valve 10 Pressure gauge 11. Buffer tank 12. Air compressor

Experimental Procedure. To evaluate the impact of liquid on the dense phase motion and the diffusion of liquid in the bed, experiments were carried out using non-evaporative silicone oil (DOW Corning, OS-30) of 1.3 cp viscosity and 0.85 specific gravity. This silicone oil has similar density and viscosity to water, but less evaporative rate (flash point of 57 °C and boiling point of 194 °C). A mass of 770 g of dry silica sand particles with an average diameter of 500 μm was used, corresponding to a static bed height of 8.6 cm. Different amount of silicone oil was premixed with dry silica sand particles, with relative volume fractions of 0.3 %, 0.6 %, 0.9 % and 1.2%, to be loaded into the fluidized bed. The experiment began when the temperature and relative humidity of air at the inlet and outlet of the fluidized bed were stable. The pressure measurement system contains two Kistler pressure sensors (Type 5015) with an accuracy of 0.01% of the full-scale span with 2000 Hz sampling frequency, placed respectively in the plenum chamber and at 3.5 cm above the gas distributor. Data were recorded for a time period of 120 s and stored in a computer using a National Instruments

data acquisition system.

3. Method of analysis

3.1 Bubble size estimation

Pressure fluctuation signals are widely used to characterize the fluid-dynamic properties of fluidized beds, i.e., bubble properties and agglomeration behaviors (Dong et al., 2015; van der Schaaf et al., 2002; van Ommen et al., 2011). van der Schaaf et al. (2002) proposed a method to calculate the bubble size based on incoherent analysis of pressure fluctuation signals. According to the van der Schaaf decoupling method, the power spectral density (PSD) of the pressure fluctuation signal at a single point can be decomposed into coherent output part (COP) and incoherent output part (IOP) by coherent analysis. The incoherent part of the power spectrum can be applied to estimate the bubble size. The IOP component was found to be caused by the rising bubbles or localized gas turbulence, corresponding to the low frequency regime. In contrast, the COP component was generated by global phenomena, such as bubble collision and eruption, and other coherent structures filtered by the IOP.

Defining the pressure fluctuation signals measured at two different positions as $p_x(t)$ and $p_y(t)$, the autopower spectrum of the signal, e.g, for $p_x(t)$ and the cross-power spectrum, are determined according to Equation (1) and Equation (2) respectively.

$$\Phi_{xx}(f) = \frac{1}{T}\left\langle F_x(f)F_x^*(f)\right\rangle \tag{1}$$

$$\Phi_{xy}(f) = \frac{1}{T}\left\langle F_x(f)F_y^*(f)\right\rangle \tag{2}$$

The coherence coefficient is defined by normalizing the absolute values of cross-power spectral density of the two signals in Equation (3), where the coherence coefficient ranges from 0-1. The pressure fluctuation signal at position y contains coherent and incoherent components with the pressure fluctuation signal at position x, where the coherent part (COP) represents the rapid pressure fluctuation inside the fluidized bed (van Willigen et al., 2003), and the incoherent part (IOP) represents the fluctuations associated with bubble motion and turbulence (van der Schaaf et al., 2002). The definition of the COP and IOP are given by Equation

(4) and Equation (5), respectively.

$$\gamma_{xy}^2 = \frac{\Phi_{xy}(f)\Phi_{xy}^*(f)}{\Phi_{xx}(f)\Phi_{yy}(f)} \tag{3}$$

$$\mathrm{COP} = \gamma_{xy}^2 \Phi_{yy} \tag{4}$$

$$\mathrm{IOP} = \left(1-\gamma_{xy}^2\right)\Phi_{yy} \tag{5}$$

According to Parseval's theorem, the integration of COP and IOP can be used to obtain the standard deviation of coherent and incoherent pressure fluctuations, as stated in Equations (6) and (7). The incoherent standard deviation of pressure pulsations is proportional to the average bubble diameter D_b at the y position.

$$\sigma_{xy,c}^2 = \int_0^\infty COPdf \tag{6}$$

$$\sigma_{xy,i}^2 = \int_0^\infty IOPdf \tag{7}$$

The relation between pressure fluctuation and bubble diameter depends on the properties of fluidized particles, bubble shape, etc. Zhang et al. (2010) and Liu et al. (2010) proposed a direct linear relation when operating at low gas velocity. The bubble size based on incoherent analysis of pressure fluctuation signals is then calculated by Equation (8), where ρ_s is the particle density and ε_{mf} is the voidage under minimum fluidization, which is estimated to be 0.4 from the experiment.

$$D_b = \sigma_{xy,i} / \left(\rho_s g\left(1-\varepsilon_{mf}\right)\right) \tag{8}$$

3.2 Attractor comparison

The attractor comparison is based on differences of the phase space reconstruction of the reference and evaluated time sequences. By calculating the embedding dimensions of the two sequences, it can be judged from the results if the original signals are generated from the same mechanism. Moreover, the statistic value, S is also applied as an indicator for the early warning of agglomeration. Typically, S>3 indicates a 95% probability that the fluidization condition has changed and agglomerates are formed (van Ommen et al., 2000):

$$S = \frac{\hat{Q}}{\sqrt{V_C(\hat{Q})}} \tag{9}$$

Where $\hat{Q}$ and $V_C(\hat{Q})$ are an unbiased estimator of the square of distances between sequences of probability distributions and the variance of the distributions, as defined in Equation (10) and Equation (11) respectively. A sequence of signal $A_k=(A_1,A_2,\ldots,A_{NA})$, which is then normalized to the reference series $X_i=(x_{i\cdot m-m+1},x_{i\cdot m-m+2},\ldots,x_{i\cdot m})$ in m embedding dimensions.

$$\hat{Q}=\frac{2}{N_1(N_1-1)}\sum_{1\le p<q\le N_1}\sum h'_{pq}+\frac{2}{N_2(N_2-1)}\sum_{N_1+1\le p<q\le N}\sum h'_{pq}-\frac{2}{N_1N_2}\sum_{p=1}^{N_1}\sum_{q=N_1+1}^{N_2}h'_{pq} \tag{10}$$

$$V_C(\hat{Q})=\frac{4(N-1)(N-2)}{N_1(N_1-1)N_2(N_2-1)N(N-3)}\sum_{1\le p<q\le N}\sum \psi_{pq}^2 \tag{11}$$

van Ommen et al. (2000) proposed a criterium for the selection of the critical parameters, band width d, segment length L and the embedding dimension m. The normalized function is applied for the combination of the delay vector and the evaluated vector, and is defined as Equation (12), where Z is a vector containing (N_X+N_Y) values.

$$h'_{pq}=\frac{1}{L^2}\sum_{i=1}^{L}\sum_{j=1}^{L}e^{-\frac{\left|z_{(p-1)L+i}-z_{(q-1)L+j}\right|^2}{4d^2}} \tag{12}$$

4. Results and discussion

4.1 Flow pattern recognition

After the liquid injection, a significant decrease of the pressure fluctuation signals with the increase of the liquid phase volume was detected. When the liquid is excessive, no bubbles are generated, and channels are formed in the fluidized bed. Fig.2. compares the original pressure fluctuation signals for dry particles and wet particles with liquid volume fractions, ω_{wl}, of 0.6% and 1.2%, at different superficial gas velocities. Fig.2.(a) shows that in the fluidized bed with liquid volume fraction above 0.6%, there are no pressure fluctuations at the measuring position. Fig.2.(b) indicates that when the fluidizing gas velocity is $2u_{mf}$ wet particles can still be fluidized normally with the liquid phase volume fraction of 0.6%, although the peak value of the original pressure fluctuation signal is lower. However, the liquid volume fraction of 1.2%, the fluctuation of the pressure signal drops sharply. Increasing the fluidizing gas velocity to $2.5u_{mf}$, the liquid-

holding capacity is enhanced and particles can be still fluidized with the liquid phase volume fraction of 0.6% and 1.2%, as shown in Fig.2.(c) and Fig.2.(d). Since the introduction of the liquid causes the formation of the liquid bridge, changing the bubble tension, both the bubble motion intensity and the bubble diameter are affected.

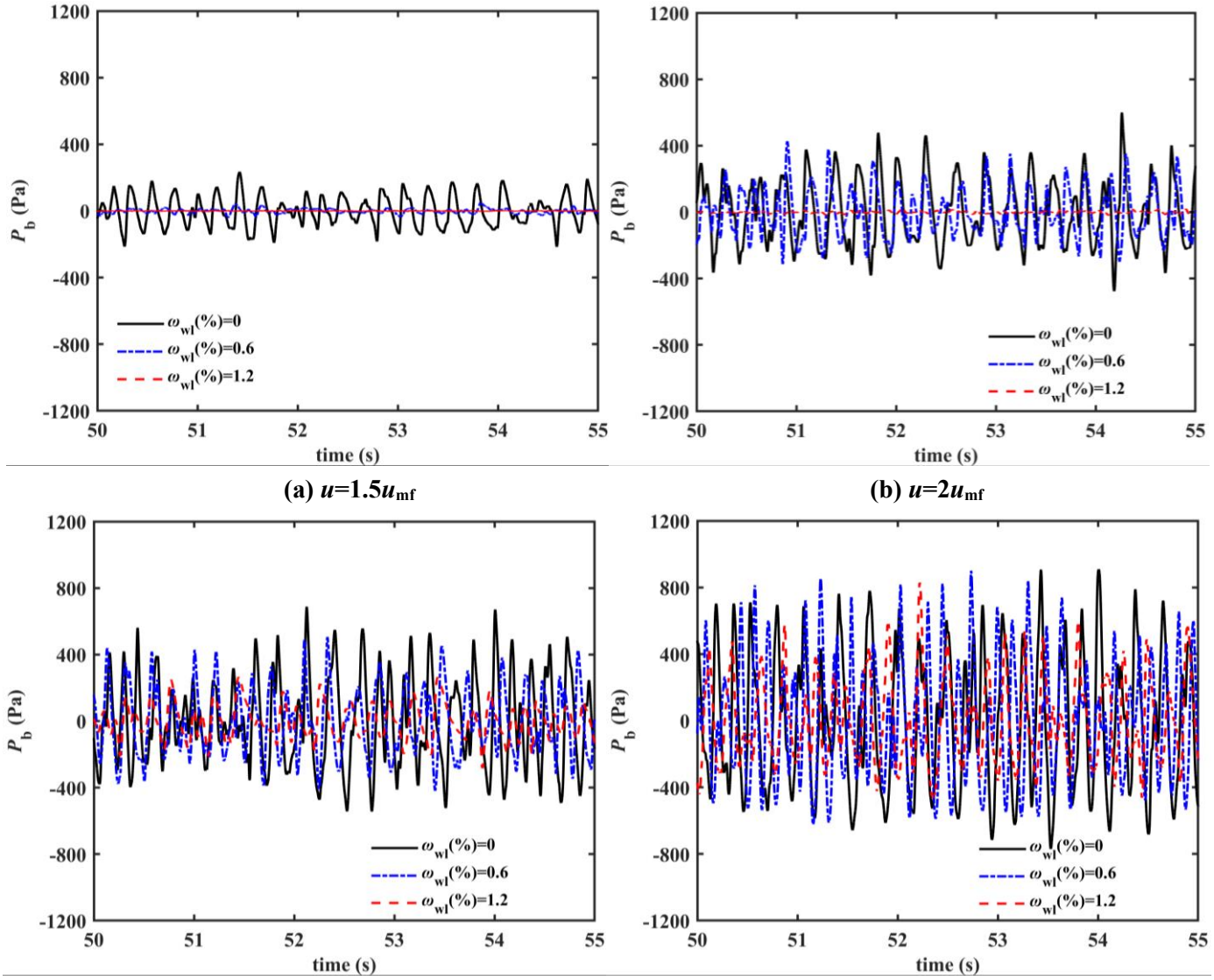

(a) u=1.5u_{mf} **(b) u=2u_{mf}**

(c) u=2.5u_{mf} **(d) u=3.5u_{mf}**

Fig.2. Pressure signals in fluidized bed of dry particles, ω_{wl} = 0, and wet particles with liquid volume fraction of 0.6 % and 1.2%.

Statistical parameters obtained from pressure signals, such as standard deviation, skewness and kurtosis are indicators of bubble size change and the transition of flow regime (Abbasi et al., 2010). Lee and Kim, (1988) found that the kurtosis and skewness of pressure signals could be used to predict the transition velocities. The probability distribution of pressure signals is a comprehensive reflection of the overall flow

behaviors, including particle-wall collision and bubble motion. The kurtosis, defined by Equation (13), quantifies the deviation of the measured signal from a normal distribution. Relatively larger values of this magnitude mean rapid change and distinct peak of signals. The skewness, defined by Equation (14) is the third central moment of the pressure signals and evaluates the lack of symmetry of the probability density function Positive and negative values of this parameter indicate longer right and left tails, respectively.

$$\text{skewness} = \frac{\sum_{i=1}^{n}\left(p_i - \overline{p}\right)^3}{(n-1)\text{STD}^3} \tag{13}$$

$$\text{kurtosis} = \frac{\sum_{i=1}^{n}\left(p_i - \overline{p}\right)^4}{(n-1)\text{STD}^4} \tag{14}$$

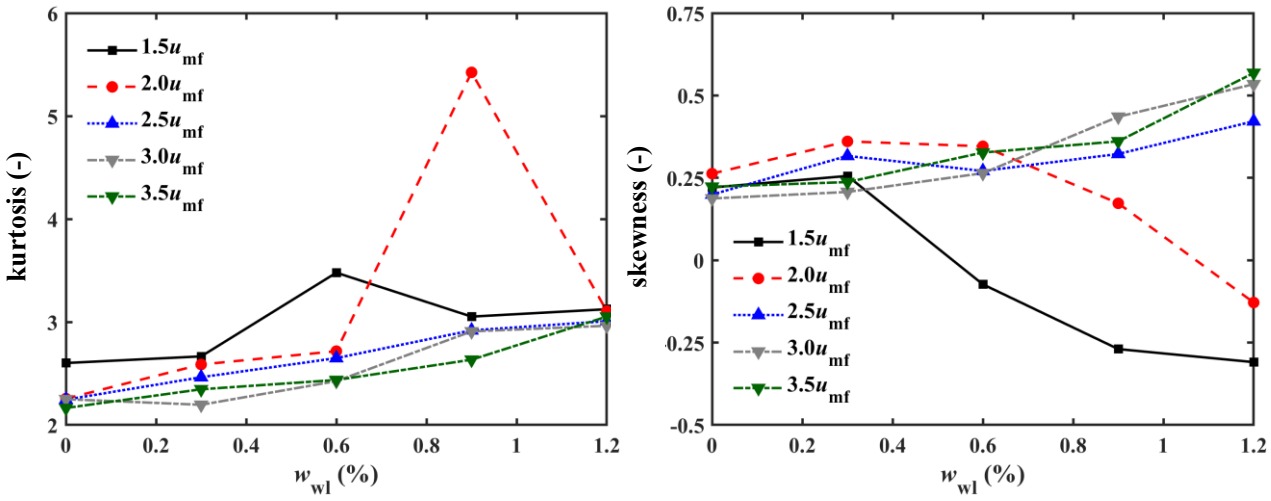

(a) Kurtosis **(b) Skewness**

Fig.3. Kurtosis and skewness results of pressure signal measured at the plenum chamber versus liquid volume fraction.

As shown in Fig.3.(a), when the fluidization velocity is 1.5u_{mf}, the kurtosis exhibits a maximum value at a liquid phase volume fraction of 0.6%. This peak of kurtosis corresponds to a liquid phase volume fraction of 0.9% for an air velocity of 2u_{mf}. According to the statistical principle, the system is a standard normal distribution when the kurtosis is equal to 3. If the kurtosis is less than 3, the time series analyzed contains more scattered points, and for values of the kurtosis above 3, the data points are more concentrated. Therefore, as shown in Fig.3.(a), when the fluidization state is abnormal, the kurtosis is much larger than 3, indicating that the pressure fluctuation signal is concentrated in this case. Combined with the analysis of the original

signal shown in Fig.2., when the liquid content is high and channels are formed, the pressure fluctuation signal still has small fluctuations, which is caused by the motion of the particles due to the local gas fluctuation in the channel. This channeling is identified by a maximum of the kurtosis, after that, for larger amounts of liquid, defluidization occurs.

Fig.3.(b) depicts the skewness of the pressure signal as a function of the liquid content. It can be seen from Fig.3.(b) that when the superficial gas velocity is $1.5u_{mf}$ with the liquid content of 0.6%, the skewness is less than 0, indicating that the distribution of the signal has shifted to the right compared to the normal distribution, and significant changes of the fluidization state have occurred. However, from the skewness curve, the critical liquid volume fraction for $2.5u_{mf}$ is 1%, which differs slightly from to what is obtained from the kurtosis analysis result. This is because the pressure signal in the fluidized bed reflects not only the bubble motion information in the bed, but contains also information like oscillations of the fluidized vessel bed itself. Furthermore, when the superficial gas velocity is larger than $2u_{mf}$, the skewness increases with the liquid volume fraction. This indicates that when the particles can be fluidized normally, the introduction of the liquid increases the bubble tension, and thus, the bubble motion becomes the main contribution to the pressure signal. As the skewness also indicates the symmetry of the pressure signal, the results in Fig.3.(b) reflect that the channels can be formed after the liquid injection, and plug-like flow might change the distribution of the pressure signal. Compared to the kurtosis, the skewness is smaller than 0 after the fluidization state of the bed is changed, so it has a high reference value for the characterization of the fluidization state. However, the kurtosis is sensitive to changes in the fluidization state, which can predict transition of the flow pattern earlier.

For low values of gas velocity and high liquid contents, the fluctuation of the pressure signal increases slightly with time, and the local particle fluctuation in the bed exhibits a star-up process, resulting in a dispersed distribution of skewness. Fig.4. shows the time evolution of the standard deviation of pressure signals, using a time period of 18 s for each calculated point. The sampled signals present stable fluidization

state within 90 s, thus, the data of the first 90 s will be used in this work.

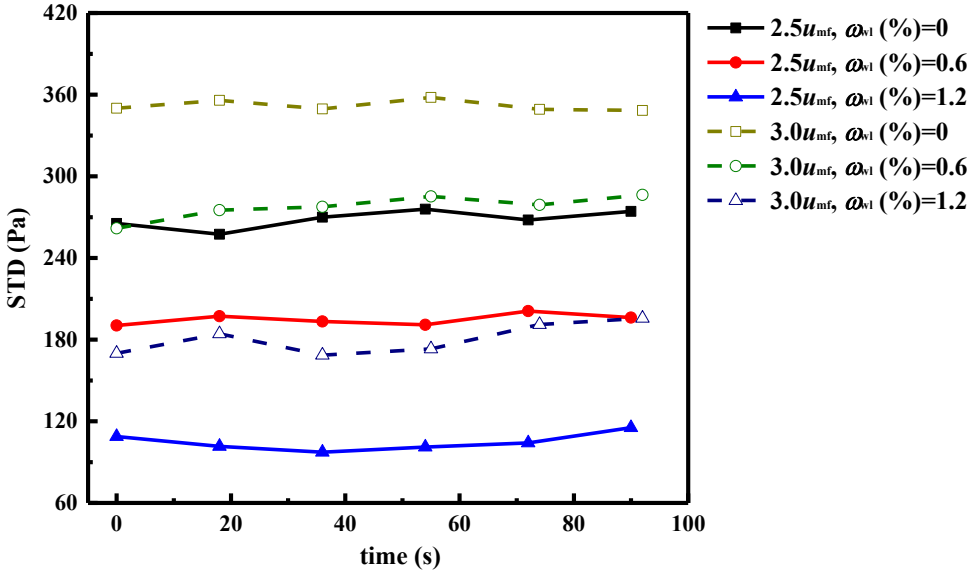

Fig.4. STD of the fluidized bed pressure fluctuation signals as a function of time.

From the previous analysis, it can be concluded that the introduction of liquid phase has a significant influence on the statistical parameters, such as the distribution of pressure fluctuation signals. To further reveal the influence of wet particles on the energy turbulence dissipation and bubble parameters in the fluidized bed, the IOP and COP spectrum of the pressure signal of the wet particle system are divided into sub-regions to distinguish and identify the flow patterns.

Fig.5. and Fig.6. show the IOP and COP spectrum, respectively. For 1.5u_{mf}, two characteristic frequency bands can be distinguished in Fig.5.(a), where the dispersion characteristics can be recognized by the slopes of the high frequency region. As stated above, at 1.5u_{mf}, when the liquid volume fraction is larger than 0.6%, bubbles in the bed disappear, so the spectrum corresponding to ω_{wl}=0.6% and ω_{wl}=1.2% have only one characteristic peak, which may be caused by local gas turbulence. In Fig.5.(b), a similar phenomenon to that observed in Fig.6.(a) can be observed in the spectrum at different liquid phase volume fractions. As bubbles disappear, the spectral characteristic peak decreases.

As the gas velocity increases (Fig.5.(c) and Fig.5.(d)), the liquid-holding capacity of the particles in the fluidized bed increases, and bubbles are present under all experimental conditions. As the liquid volume fraction increases, the frequency of bubbles in the wet particle system decreases due to an increase of the

surface tension of the bubble. The spectrum in the higher frequency band is attenuated by power law, indicating that the frequency band is related to particle motion caused by bubbles (van Wachem et al., 1998).

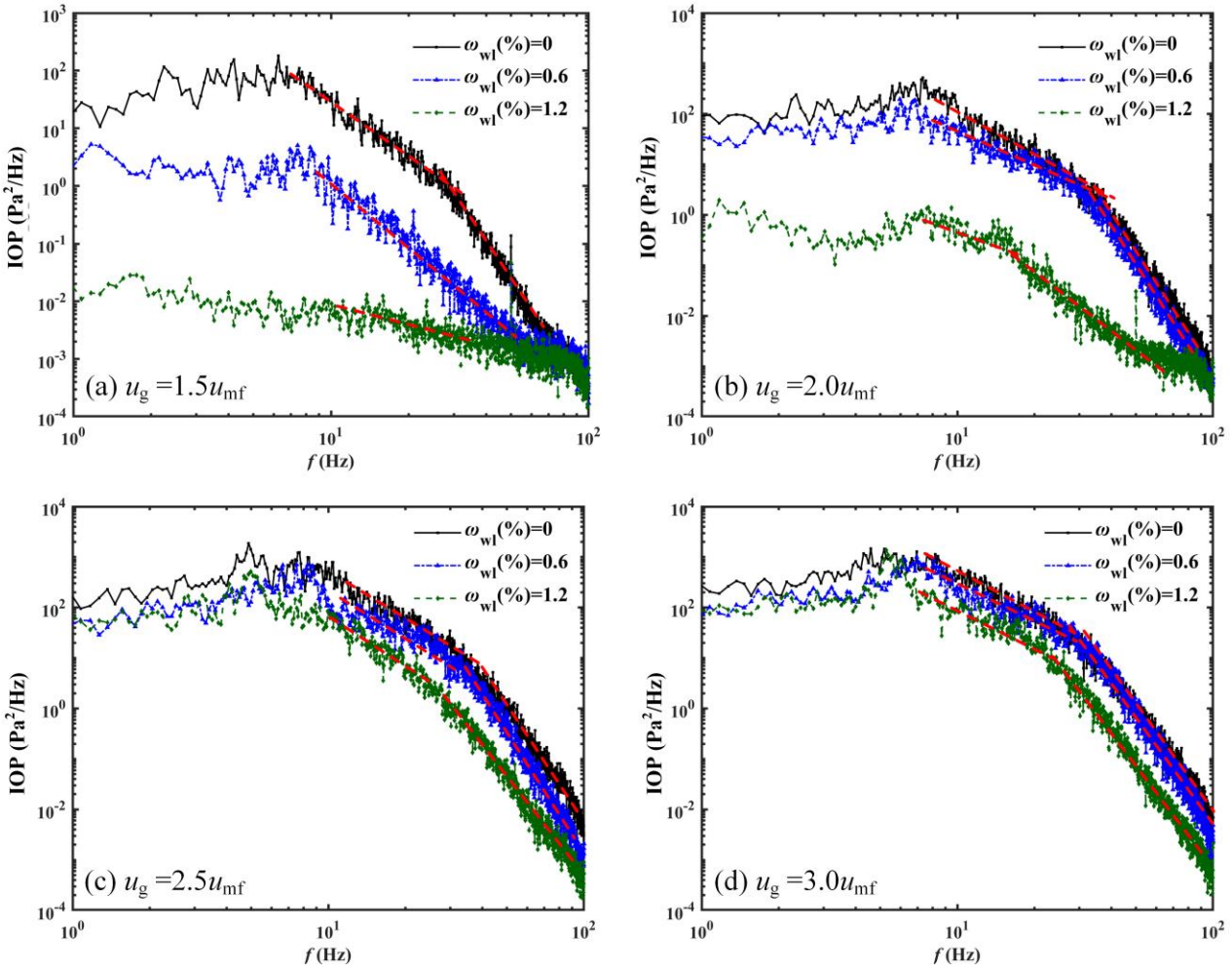

Fig.5. IOP of the pressure fluctuation signals under different gas velocities with liquid volume fractions of ω_{wl}=0 %, 0.6% and 1.2%.

The COP spectra depicted in Fig.6. show the composition and source of pressure fluctuations. For the dry particles case, bubble formation and coalescence processes can be identified from the characteristic peaks of the spectrum. Since the superficial gas velocity in Fig.6.(a) is low, particle agglomerates or discrete small bubbles may be formed in the fluidized bed in this case and several characteristic peaks can be found. When the liquid volume fraction is larger, the characteristic peak of COP decreases, which may be a consequence of a change in flow mode and due to non-uniformity in the bed caused by the propagation of pressure waves. The results show that at the superficial gas velocity of 1.5u_{mf} and 2u_{mf}, the signals detected by the pressure

sensor include typical pressure sources, such as fluidized bed radial fluctuations (van Ommen et al., 2004). As shown in Fig.6.(b), for a higher superficial gas velocity, the bubble motion in the bed becomes more vigorous, the bubble diameter becomes larger, and the mixing in the fluidized bed is enhanced. In this case, the liquid-holding capacity in the fluidized bed increases, and the influence of the liquid bridge on the particle flow is smaller than the drag force of the particles and, thus, the flow characteristics are not significantly changed. The results presented in Fig.5. and Fig.6. reflect that the transition of the flow mode and the disappearance of the characteristic structure in the fluidized bed can be detected using the spectrum of the fluidized bed of wet particles.

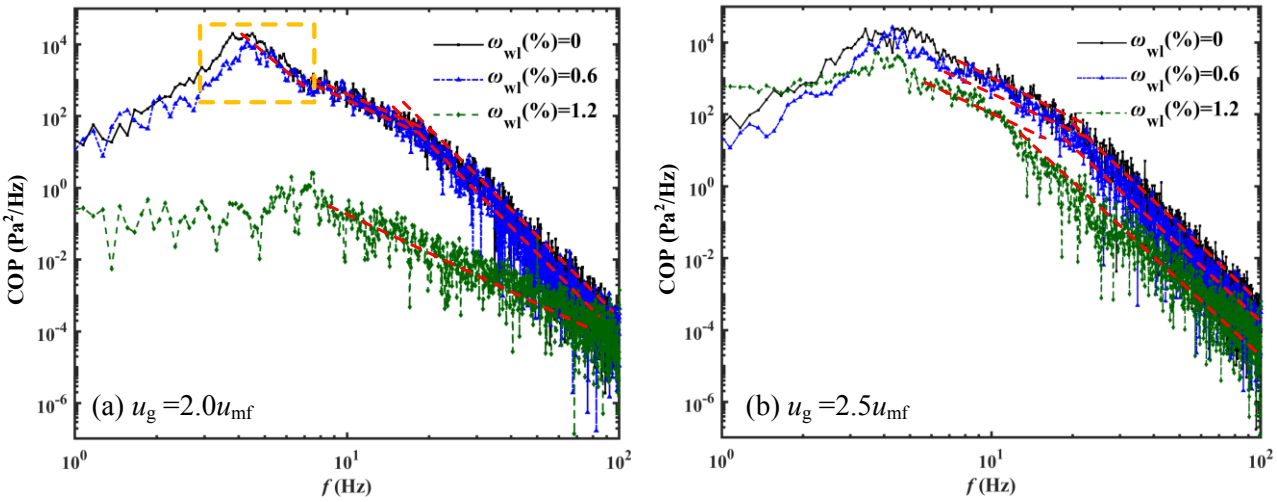

Fig.6. COP of the pressure fluctuation signals under different u_g with ω_{wl}=0 %, 0.6% and 1.2%.

Sun et al. (2011) observed that the energy spectrum could be divided into energy-containing range, inertial range, and dissipation range. The slope of the spectrum in the inertial range was characterized by the Levy-Kolmogorov index, which is an indicator of flow intermittency. Nevertheless, the Levy-Kolmogorov law can be applied to identify the subregions in the high Reynolds number regime, whereas the Kolmogorov law can be used for the range of relatively lower Reynolds number regime. The power-law decay with increasing frequency was calculated by means of power spectra of pressure signals by van Wachem et al. (1999). The decay index or scaling index can be calculated by the slope of the inertial segment of Fig.5.

The results of the scaling index as a function of the gas velocity are shown in Fig.7 for various liquid

volume fractions. For superficial gas velocities of 1.5u_{mf} and 2u_{mf}, the scaling index is between -5/3 and -1, which indicates that the flow turbulence is weak and the laminar flow behavior dominates. Considering the result in Fig.5.(a), where the IOP of the pressure signals with liquid volume fraction of 1.2% only presents one peak, no energy dissipation because of the appearance of bubbles is found in this case. According to Chen and Zhou, (2005), an anomalous diffusion of flow behaviors is observed when the scaling index is between -5/3 and -1. Under these conditions, the flow is characterized by a Brownian motion resulting from the fractional Laplacian dissipation, indicating weak or even no turbulence. The flow intermittency of turbulence characterized by the Levy stability index can be transformed into the decay index. The critical value of decay index is -3, indicating that another flow pattern exists for the decay indexes between -3 and -5/3. The decay index in Fig.7 increases with the liquid volume fraction, indicating a decrease in particle turbulence. However, under the same liquid volume, if the flow pattern does not change, the effect of the superficial gas velocity on the decay index is negligible, which means that the particles are still in the turbulent state.

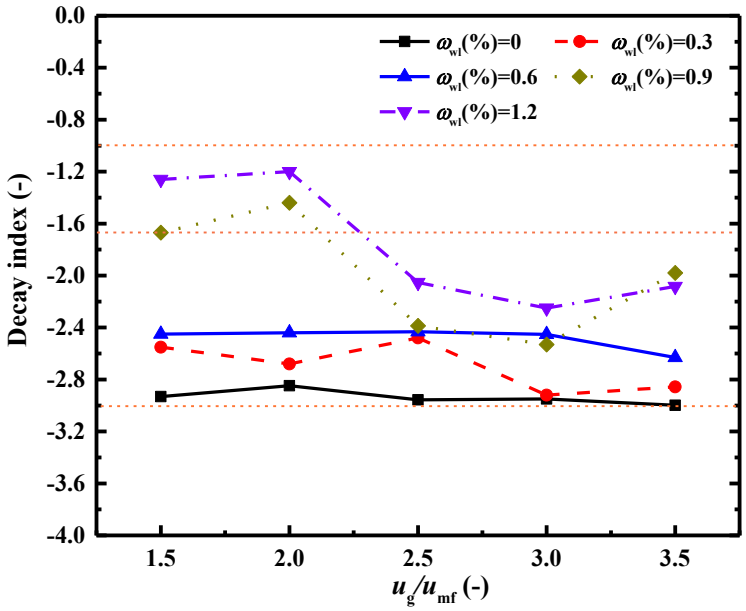

Fig.7. Decay index of the incoherent power spectrum.

4.2 Bubble diameters in wet particle fluidized beds

The standard deviation (STD) of pressure signals is an indicator of the bubble size and the peak value of the power spectrum can also be used to estimate the strength of the bubble motion in the liquid injection

system (Gómez-Hernández et al., 2012; Zhou et al., 2013b). Along with kurtosis and skewness, the standard deviation can also be used to predict the transition of the flow pattern. In Fig.8., the STD of the pressure signals measured in the bed are shown. The magnitude of standard deviation decreases with the liquid volume fraction. For $1.5u_{mf}$ and $2u_{mf}$, the bubble diameter is significantly reduced and the defluidization occurred for liquid volume fractions above 0.3% and 0.6%, respectively. Considering the linear increase of the STD with the gas velocity, typically used to determine the minimum fluidization velocity, an effect of the liquid volume fraction on u_{mf} can be observed in Fig.8. The apparent minimum fluidization velocity of wet particles increases with the liquid volume fraction.

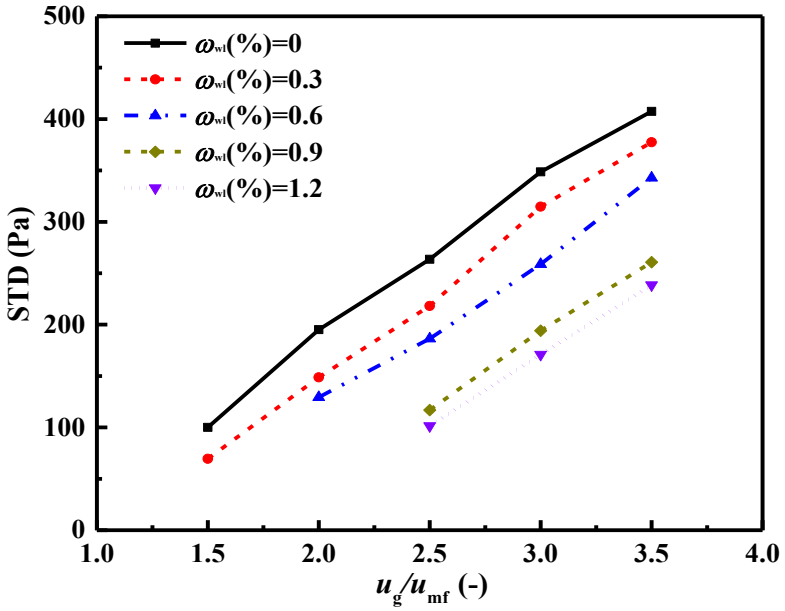

Fig.8. Standard deviation of the fluidized bed pressure signal with increasing gas velocity.

As stated previously, the bubble diameter can be estimated by the incoherent analysis, being the pressure in the plenum chamber the overall indicator of the fluidized condition. The bubble diameter calculated by the incoherent analysis (COA) is plotted in Fig.9, together with the correlations of Kato and Wen (1969), Yasui and Johanson (1958) and Darton et al. (1977) for comparison. These correlations are given by Equation (15), Equation (16) and Equation (17), respectively.

$$D_b = 0.014\rho_s d_p \left(\frac{u_g}{u_{mf}}\right) h \qquad (15)$$

$$D_b = 0.03274\rho_s d_p \left(\frac{u_g}{u_{mf}} - 1\right)^{0.63} h \quad (16)$$

$$D_b = 3.9\rho_s^{0.4} d_p^{0.8} \left(\frac{u_g}{u_{mf}} - 1\right)^{0.4} h^{0.8} \quad (17)$$

In Fig.9.(a), fairly good agreement can be seen between the COA and the correlation values. For lower superficial gas velocity, the bubble diameters calculated by COA are slightly smaller than the theoretical values derived from the correlations, probably due to the wall effect. For velocities higher than $2.5u_{mf}$, the COA results and the calculated values by the model of Yusui and Johanson are similar, since this model considers the gas cavity. In Fig.9.(b), the injection of the liquid leads to a decrease of the bubble diameter. It is worth noticing that for $1.5u_{mf}$ with 0.6%, small bubbles with average diameters of 2.5 mm are formed and the turbulence caused by localized bubble rising and gas changes the flow regime of the fluidized bed. However, as shown in Fig.7., standard deviation of pressure signals are about 10 Pa in the plenum chamber and 0 Pa in the fluidized bed, which indicates that there are almost no bubbles in the fluidized bed.

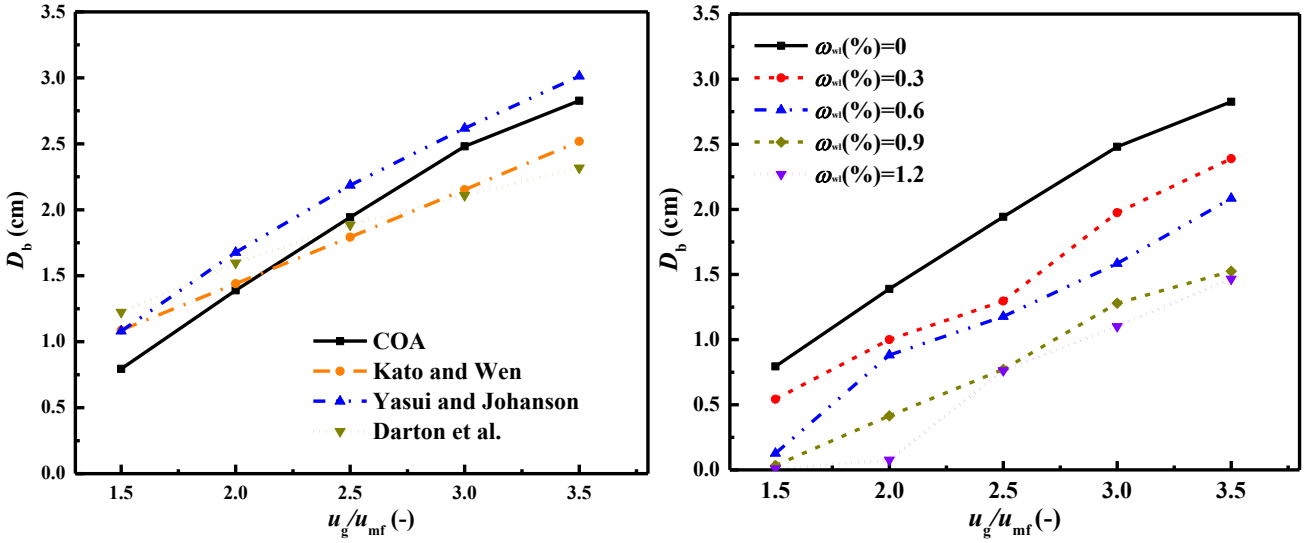

Fig.9. (a) Comparison of measured bubble diameter (COA) with values derived from correlations. (b) Influence of liquid content and superficial gas velocity on bubble diameter

The minimum fluidization velocity of particles is affected by the liquid fraction, as stated in the analysis of Fig.8. This minimum fluidization velocity can be obtained for the wet particle system from the linearization

of the STD of the pressure signal (Fig.8). Afterwards, u_{mf} for wet particles systems containing different liquid volume fractions are used in the empirical correlations to recalculate bubbles diameters. The results are shown in Fig.10. Although the empirical correlations consider no liquid bridge force, the results derived from the correlations still show similar trends to the experimental results. This indicates that the global bubble behavior is directly related to the gas and particle turbulence.

Seville and Clift (1984) found that the liquid bridge force could alter the fluidization characteristics of Geldart B classification particles, which could behave as Geldart A or C particles. Wormsbecker and Pugsley (2008) observed a similar phenomenon in the drying process of pharmaceutical particles, i.e., the particles showed local defluidization and channels were formed for high humidity content, showing a fluidized behavior typical of Geldart C particles. Therefore, in contrast to gas-solid two-phase system, the particle fluctuation cannot be characterized by bubble dynamics for wet particle systems. The cohesive force significantly changes the particle fluctuation. For instance, the decay index showed that for 0.9% liquid volume fraction at $2u_{mf}$, the flow pattern of particles had already been changed. The transition points, corresponding to $2.5u_{mf}$ and $2u_{mf}$ in Fig.10.(a) and Fig.10.(b), respectively, also show the effect of liquid injection.

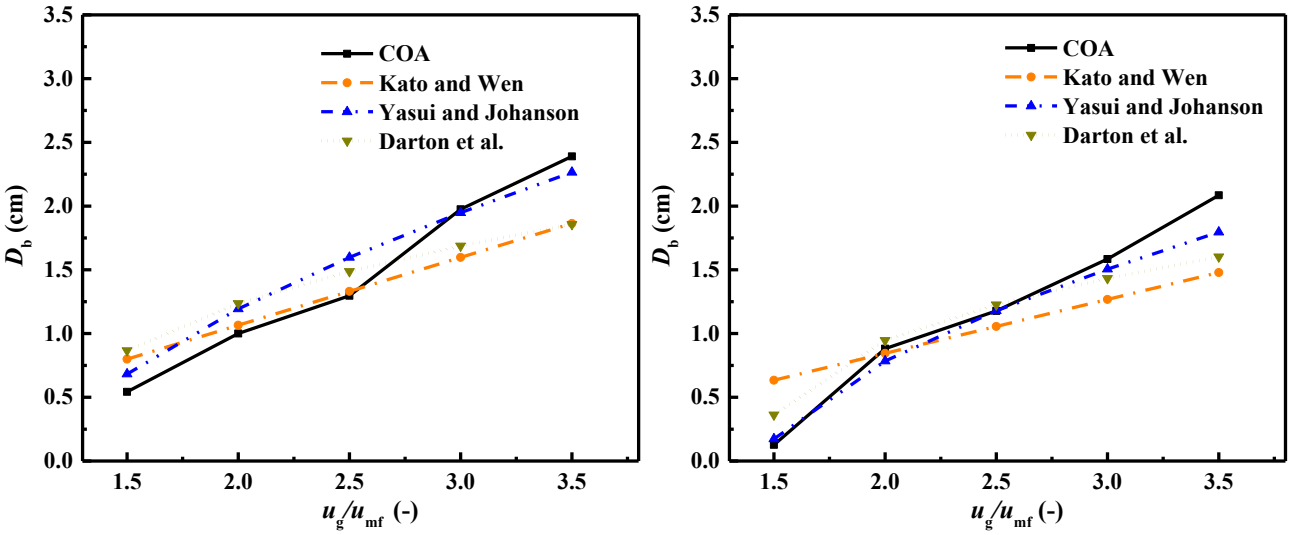

(a) ω_{wl}=0.3 %　　(b) ω_{wl}=0.6 %

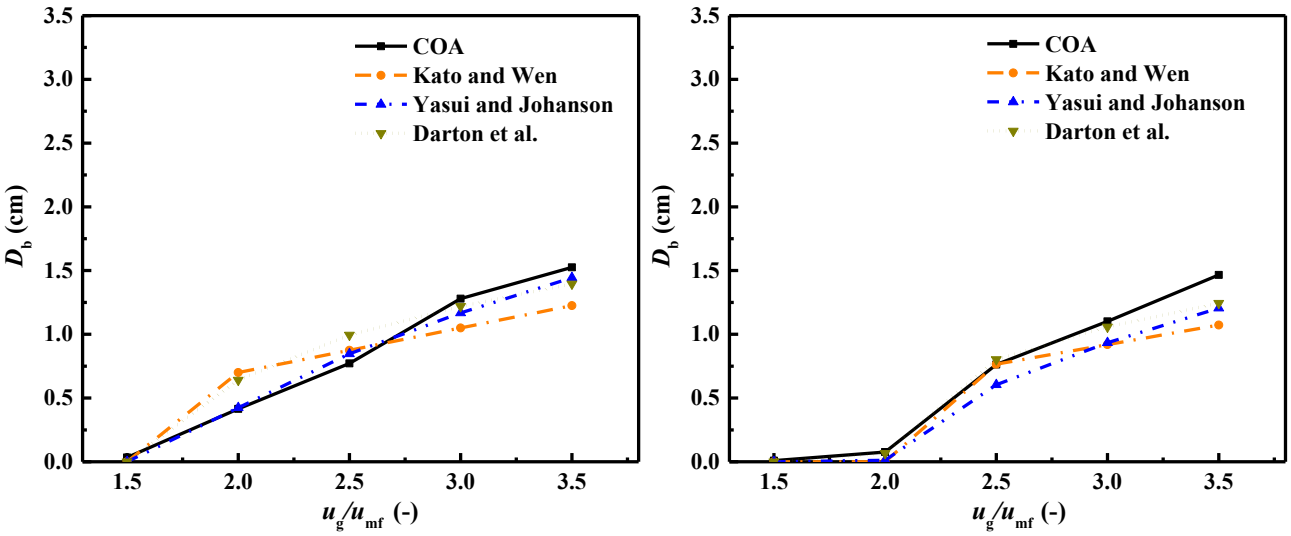

Fig.10. Comparison of bubble diameters measured experimentally for wet particles with correlations.

McLaughlin et al. (2001) found that increasing the amount of liquid in the fluidized bed, the interparticle liquid bridge force gradually increased and replaced van der Waals forces to became the dominant forces in the bed. The fluidization characteristics of the particles changed from Geldart B to Geldart A particles and, finally, a behavior typical of Geldart C particles was found. The transition boundary between Geldart $\overline{BA}$ and $\overline{AC}$ is closely related to the ratio of liquid bridge force between particles to fluid drag. They evaluated the influence of the liquid volume adding to the fluidized system and found that the ratio of the fluid drag force to the liquid bridge force was directly related to the change of the particle classification. Therefore, to further understand the flow transition behavior, a force analysis is required.

The liquid bridge force between particles can be divided into static liquid bridge force and dynamic liquid bridge force (Seville et al., 2000). The static liquid bridge force is mainly related to the surface tension and the geometry of the liquid bridge and is calculated by Equation (18) (Adamsand and Perchard, 1985), where σ is the surface tension and θ is the liquid-solid contact angle for determining the wetting property of the liquid. θ can be determined by the liquid surface energy γ_l and the solid surface energy γ_s (Popov, 2010), as shown in Equation (19).

$$F_s = \pi d_s \sigma \sin\phi \sin(\phi+\theta) + \frac{\pi d_s^2}{4}\Delta P \sin^2\phi \qquad (18)$$

$$\cos\theta = 2\sqrt{\frac{\gamma_s}{\gamma_l}} - 1 \tag{19}$$

In Equation (18), ϕ is the half-filling angle and is calculated by Equation (20), where ω is the saturability and is equivalent to the liquid volume fraction ω_{wl}, C_a and C_δ are the correction factors (Weigert and Ripperger, 1999), and ΔP is a parameter related to the curvature of the gas-liquid interface, which is difficult to calculate accurately, but can be neglected in most cases (Seville et al., 2000).

$$\phi = \arcsin\left[\left(\frac{\omega}{0.36}\frac{\varepsilon^2}{1-\varepsilon}\frac{1}{C_a C_\delta}\right)^{0.25}\right] \tag{20}$$

The dynamic liquid bridge force is related to the liquid viscosity and particle movement. The relative magnitudes of the dynamic liquid bridge force (Ennis et al., 1990) can be estimated by Equation (21):

$$F_{\mathrm{d}} = \frac{3}{8}\pi d_{\mathrm{s}}^2 \mu f_{\mathrm{os}} \sin^2\phi \tag{21}$$

Where f_{os} is the characteristic oscillation frequency of the system. As θ can be neglected, then the liquid bridge force can be expressed as Equation (22) (McLaughlin and Rhodes, 2001).

$$F_{\mathrm{liq}} = \pi d_s \sigma \sin^2\phi + \frac{3}{8}\pi d_{\mathrm{s}}^2 \mu f_{\mathrm{os}} \sin^2\phi \tag{22}$$

The gravitational force of particles is calculated by Equation (23).

$$F_{\mathrm{g}} = \frac{\pi d_{\mathrm{s}}^3}{6}\rho_{\mathrm{s}}\mathrm{g} \tag{23}$$

For $Re_p \leq 0.7\text{-}4$ and $0.4 < Re_p < 700$, the drag coefficient can be calculated respectively by Equation (24) and Equation (25), respectively, whereas for $700 < Re < 2\times10^5$, C_D is equal to 0.44. Therefore, the drag force of particles can be calculated by Equation (26).

$$C_D = \frac{24}{Re}\left(1 + \frac{3}{16}Re\right) \tag{24}$$

$$C_{\mathrm{D}} = 18.5/Re^{0.6} \tag{25}$$

$$F_{\mathrm{d}} = \frac{1}{2}C_{\mathrm{D}}\rho_{\mathrm{g}}(u_{\mathrm{g}} - u_{\mathrm{s}})^2\frac{\pi d_{\mathrm{s}}^2}{4} \tag{26}$$

Where $(u_g\text{-}u_s)$ can be characterized and estimated as the slip velocity. The drag coefficient described

above is for calculating single particle drag coefficients. However, due to the interaction between particles and their neighboring, the apparent drag coefficient of particle groups may differfrom the drag coefficient of individual particles due to unstable fluid flow, turbulence, compressibility, etc. Therefore, the drag coefficient needs to be corrected. Since the measurement of the drag force of particle groups is far more difficult than the measurement of the drag force of a single particle, there are few reports on the drag force of particle groups. For the dense phase fluidized bed, Wen and Yu (1966) proposed a calibrated correlation to describe the apparent drag coefficient of particle groups and the calibrated drag force can be calculated using C_{Da} from Equation (27). In the present work, it is assumed that under the same superficial gas velocity, dry particles and wet particles have the same drag forces and are both calculated by Equation (28).

$$C_{\mathrm{Da}} = C_{\mathrm{D}} \varepsilon^{-4.7} \tag{27}$$

$$F_{\mathrm{d}}^{*} = \frac{1}{2} C_{\mathrm{Da}} \rho_{\mathrm{g}} (u_{\mathrm{g}} - u_{\mathrm{s}})^{2} \frac{\pi d_{\mathrm{s}}^{2}}{4} \tag{28}$$

The liquid bridge and drag forces are compared in Fig.11., where the upper *x*-axis represents the liquid volume fraction and the dashed horizontal lines shows the drag force under each superficial gas velocity. The calibrated drag force, based on the drag force of the single particle, takes the particle volume fraction into account. Further details of the calculation procedure can be found in a previous work (Zhou et al., 2017). The competition effect of the liquid bridge force is clearly seen in Fig.11. For instance, for $1.5u_{mf}$, the liquid bridge becomes dominant for liquid volume fractions higher than 0.3%, whereas a liquid volume fraction of at least 0.6% is required to have a dominant effect of liquid bridge forces when the bed is fluidized at $2u_{mf}$.

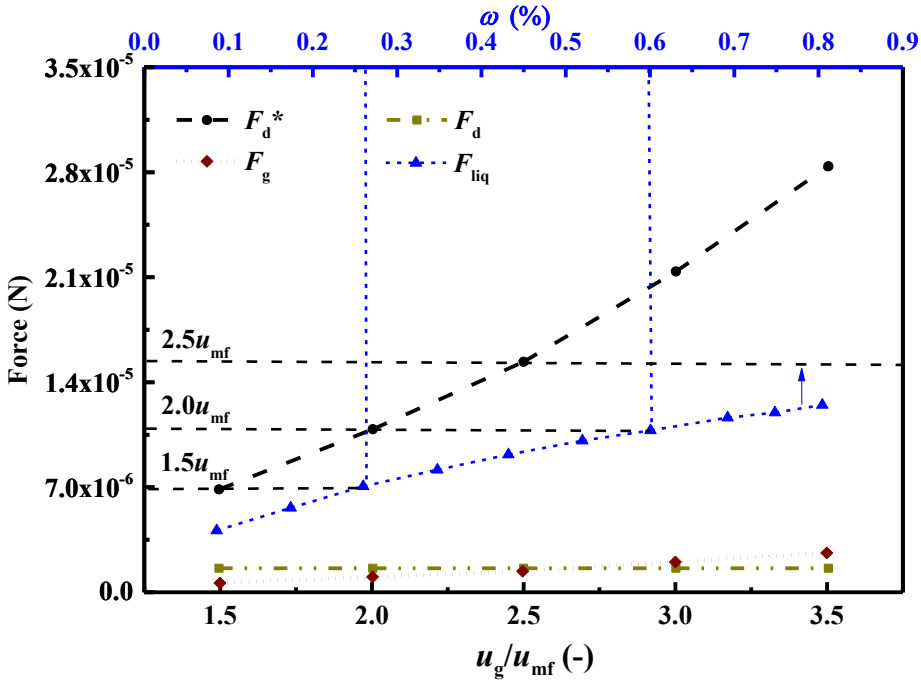

Fig.11. Force analysis of wet particle fluidized beds.

4.3 Continuous wavelet analysis

As established by Briongos et al. (2006), pressure signals contain information of particle, bulk and global bubble dynamics, where the particle dynamics generated by particle-wall and particle-particle collision are within the frequency range 0-20 Hz. By the coherent and incoherent power spectrum analysis, the dominant peaks responsible of the bubble behaviors, were obtained. However, the particle dynamics and the particle-wall interaction are also contained in the pressure signals and, thus, understanding the frequency range affected by particle dynamics is also relevant. As proposed by Gómez-Hernández et al. (2012), a spectrum density diagram can be applied to identify the flow regime change during liquid injection in a fluidized bed. Sun et al. (2012) also applied auto-correlation of wavelet coefficients ichnography of the fluidized bed loaded with polyethylene particles and found that the coefficients were related to the kernels of particle vortexes and boundaries of two vortexes, and could also reflect the effect of bubble interactions on the particle vortex. The characteristic frequency and the corresponding power in the time series was clearly seen and identified in the 2D spectrum. However, continuous wavelet transformation analysis (CWTA) is capable of monitoring the local singularity, which might contain useful information apart from global fluidization behavior and, thus, is

chosen for the following study.

The CWTA is defined in Equation (29) (Mallat, 1999), where a is the scaling factor, b is the location factor, ψ and ψ^* are the mother wavelet function, which is the Morlet wavelet in this study, and its conjugate value. Analytic wavelets are complex-valued wavelets whose Fourier transform vanishes for negative frequencies. As the wavelet coefficients are complex numbers, they contain information ofphase position and magnitude of the signal being analyzed (Sasic et al., 2006). In Fig.12, the color scale represents the power and the vertical coordinate represents the frequency.

$$CWf(a,b) = \langle f, \Psi_{a,b} \rangle = \frac{1}{|a|^{1/2}} \int f(t) \Psi^* \left(\frac{t-b}{a} \right) \mathrm{d}t \tag{29}$$

When there is no liquid present in the fluidized bed, the pressure wave caused by bubble eruption is observed to be periodical at around 4.5 Hz, as can be seen in Fig.12(a), (d) and (g). When the superficial gas velocity increased to $3u_{\mathrm{mf}}$, the bubble eruption and rising become violent and disordered, therefore the dominant frequency increases and the frequency distribution becomes wider. As the superficial gas velocity is further increased to $3.5u_{\mathrm{mf}}$, the main frequency is at around 5.2 Hz, indicating that the bubble motion intensity increases and the flow pattern tends to be stable. With the injection of liquid, as shown in Fig.12.(b), (e) and (h), the energy in the high frequency region increases. As time progresses, the peak of the main frequency increases in this case, and a new characteristic peak structure appears at approximately 7.5 Hz.

Although the diameter of bubbles is significantly reduced after the liquid injection, the continuous wavelet analysis shows that the energy of the high-frequency zone increases rapidly with the volume fraction of liquid 0.6% at $3.5u_{\mathrm{mf}}$. However, for $2u_{\mathrm{mf}}$ and $2.5u_{\mathrm{mf}}$, the trend is slower. This phenomenon indicates that, as fluidization progresses, characteristic structures like agglomerates appear in the bed. When the liquid volume fraction is low or there is no liquid, higher gas velocities lead to stronger turbulence of bubbles, enhancing mixing of particles. Since the silicone oil used in this system is a non-volatile liquid, the particle agglomeration process is greatly accelerated. The formation of agglomerates also leads to a change in the

particle classification, as discussed previously, so the frequency of bubble's motion and breakage also change. Fig.13.(c), (f) and (d) reflect an increase in the frequency region of 2-3 Hz as the time progresses and the fluidizing gas velocity increases. The appearance of features at this location might be related to unstable local flow aggregates.

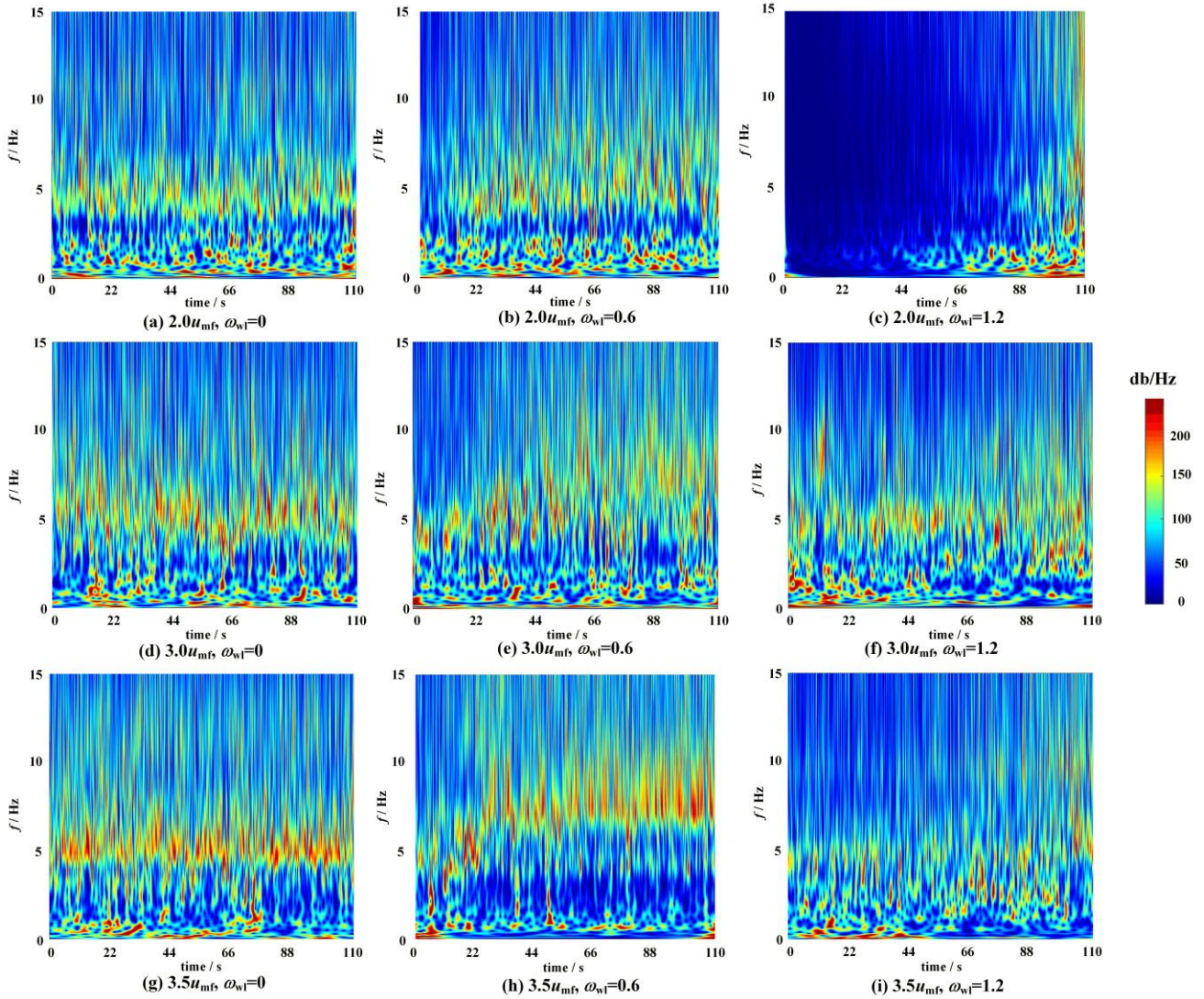

Fig.12. Continuous wavelet analysis of the fluidized bed signal for various liquid volume fractions.

4.4 Attractor analysis

Fig.13. shows the statistical parameter *S* as a function of liquid phase volume fraction, using the pressure signal for dry particles as the reference time series for attractor comparison. When *S* exceeds 3, the fluidization behavior becomes abnormal and there is a tendency to agglomeration. According to Equations (10) and (11), *S* is calculated based on the distances between two distributions (Equation (9)). When *S*>3, there is a 95%

certainty of denying the hypothesis of same distribution. The window time is selected based on the main frequency of the power density spectrum, which affects the calculation time and the optimized window time is usually from 1/3 to 1/4 of the characterized cycle. The embedding dimension is set to 11, calculated by the correlations of $T_w F_s$=2m, where F_s is the resample frequency of 200 Hz. The band width is set to 0.01 and the segment length is set to 14 s, which meets the requirement of containing several cycles in the sampling period.

For a liquid volume fraction of 0.3%, the formation of agglomerates is not detected in Fig.13, i.e., S is below 3 independently of the liquid volume fraction analyzed. The addition of liquid mainly affects the bubble motion and the particle fluctuation. Increasing of the liquid volume fraction, for $1.5u_{mf}$, $2u_{mf}$ and $2.5u_{mf}$, the tendency of agglomeration formation is clearly observed. It should be noticed that for $2.5u_{mf}$ with 0.6% liquid volume fraction, S is 4 and 1 in the fluidized bed and in the plenum chamber, respectively. In the lower part of the fluidized bed, the localized particle motion and particle mixing is seriously affected by the presence of liquid and shows the tendency to agglomeration. However, in the plenum chamber, the defluidization of the lower part of the bed is not fully detected.

Considering the pressure signal measured in the bed, no agglomeration is detected when fluidizing the bed at $3u_{mf}$ and $3.5u_{mf}$, independently of the liquid volume fraction tested. For these high gas velocities, the vigorous fluidization can break any small agglomeration generated. However, the smooth fluidization resulting for gas velocities below $3u_{mf}$ may lead to agglomeration problems for liquid volume fractions above 0.6%.

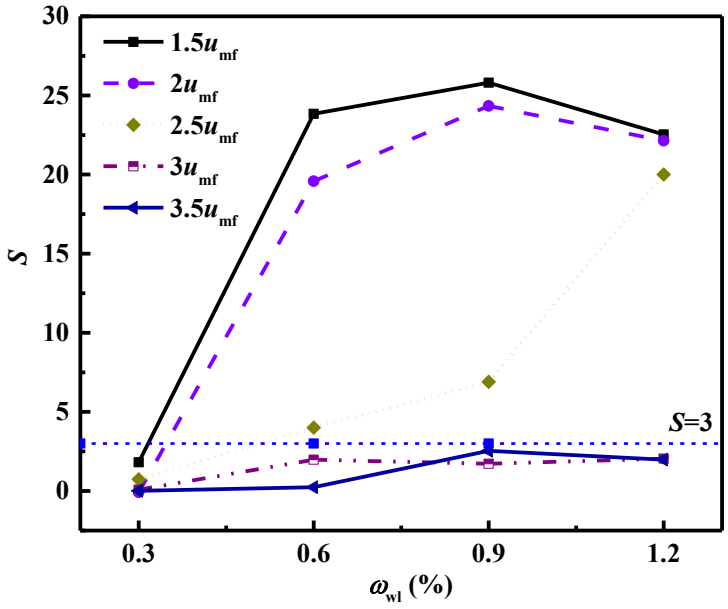

Fig.13. Attractor analysis for detecting agglomeration problems in fluidized beds conformed by dry and wet particles.

5. Conclusions

In this work, the bubble dynamics of wet particle fluidized beds is studied. Non-volatile silicone oil was used as the wetting medium for the experimental measurements. Pressure fluctuation signals in the plenum chamber and in the bed under different conditions were analyzed. The results show that the incoherent algorithm can detect the bubbles in the high liquid content system, and the standard deviation of the pressure fluctuation signal is not sensitive to the detection of small bubbles. The critical transition condition of the flow pattern from turbulent to laminar flow can be obtained from the kurtosis and skewness of the pressure signal. Through the decay index analysis of the incoherent spectrum, the operating region of the Levy-Kolmogorov flow pattern to the Kolmogorov flow pattern under different liquid volume fractions is obtained. Furthermore, through force analysis, the result indicates that the competitive mechanism of liquid bridge and drag forces is the potential reason for the change of apparent minimum fluidization of wet particles. However, the liquid bridge force not only changes the particle properties and the bubble behaviors, but also leads to a higher chance of forming agglomerates in the fluidized bed.

Notations

a scaling factor

b	location factor
C_a,C_δ	correction factors
D_b	bubble diameter
d_p	particle diameter
d	band width
F	Fourier transform of the pressure signal
F_s	static liquid bridge force
F_d	dynamic liquid bridge force
f_{os}	characteristic bed frequency
f	frequency
h	bed height
L	segment length
m	embedding dimension
P_b	pressure of the fluidized bed
$\hat{Q}$	unbiased estimator of the square of the distances
S	attractor
T_w	window time
u_0	superficial gas velocity
u_s	particle velocity
u_{mf}	minimum fluidization velocity
$V_C(\hat{Q})$	variance of the distributions
Φ	PSD of the pressure signal
σ	surface tension
ρ	density
ε	voidage
ω_{wl}	liquid volume fraction
ω	saturability
ϕ	half-filling angle
ψ,ψ^*	mother wavelet function and its conjugate value
θ	liquid-solid contact angle

γ_l liquid surface energy

γ_s solid surface energy

γ coherence coefficient

μ viscosity

Subscript

s solid

c, i coherent and incoherent parts

x,y measuring position

Abbreviation

COA coherent analysis

CWTA continuous wavelet transformation analysis

FCC fluid catalytic cracking

G-L-S gas-liquid-solid

G-S gas-solid

STD standard deviation

References

Abbasi, M., Sotudeh-Gharebagh, R., Mostoufi, N., Zarghami, R., Mahjoob, M.J., 2010. Nonintrusive characterization of fluidized bed hydrodynamics using vibration signature analysis. AIChE Journal 56, 597-603.

Adamsand M. J., Perchard, V., 1985. The cohesive forces between particles with interstitial liquid. Inst. Chem. Eng. Symp. Series 91, 147.

Bacelos, M.S., Passos, M.L., Freire, J.T., 2007. Effect of interparticle forces on the conical spouted bed behavior of wet particles with size distribution. Powder Technology 174, 114-126.

Bouffard, J., Bertrand, F., Chaouki, J., Giasson, S., 2012. Control of particle cohesion with a polymer coating and temperature adjustment. AIChE Journal 58, 3685-3696.

Briongos, J.V., Aragón, J.M., Palancar, M.C., 2006. Phase space structure and multi-resolution analysis of gas-solid fluidized bed hydrodynamics: Part I—The EMD approach. Chemical Engineering Science 61, 6963-6980.

Chen, S., Fan, Y., Yan, Z., Wang, W., Liu, X., Lu, C., 2016. CFD optimization of feedstock injection angle in a FCC riser. Chemical Engineering Science 153, 58-74.

Chen, W., Zhou, H.B., 2005. Levy-Kolmogorov scaling of turbulence. Mathematics.

Darton, R.C., La Naueza, R.D., Davidson, J.F., Harrison, D., 1977. Bubble growth due to coalescence in fluidized beds. Transactions of the Institution of Chemical Engineers 55, 274-280.

Dong, K., Zhang, Q., Huang, Z., Liao, Z., Wang, J., Yang, Y., 2015. Experimental investigation of electrostatic effect on bubble behaviors in gas-solid fluidized bed. AIChE Journal 61, 1160-1171.

Eliaers, P., De Wilde, J., 2013. Drying of Biomass Particles: Experimental Study and Comparison of the Performance of a Conventional Fluidized Bed and a Rotating Fluidized Bed in a Static Geometry. Drying Technology 31, 236-245.
Ennis, B.J., Li, J., Gabriel I, T., Robert, P., 1990. The influence of viscosity on the strength of an axially strained pendular liquid bridge. Chemical Engineering Science 45, 3071-3088.
Gómez-Hernández, J., Soria-Verdugo, A., Briongos, J.V., Santana, D., 2012. Fluidized bed with a rotating distributor operated under defluidization conditions. Chemical Engineering Journal 195, 198-207.
Gao, J.S., Xu, C.M., Lin, S.X., Yang, G.H., Guo, Y.C., 2001. Simulations of gas-liquid-solid 3-phase flow and reaction in FCC riser reactors. Aiche Journal 47, 677-692.
Kato, K., Wen, C.Y., 1969. Bubble assemblage model for fluidized bed catalytic reactors. Chemical Engineering Science 24, 1351-1369.
Lee, G.S., Kim, S.D., 1988. Pressure fluctuations in turbulent fluidized beds. Journal of Chemical Engineering of Japan 21, 515-521.
Liu, M., Zhang, Y., Bi, H., Grace, J.R., Zhu, Y., 2010. Non-intrusive determination of bubble size in a gas–solid fluidized bed: an evaluation. Chemical Engineering Science 65, 3485-3493.
Mallat, S., 1999. A wavelet tour of signal processing. Elsevier.
McLaughlin, L.J., Rhodes, M.J., 2001. Prediction of fluidized bed behaviour in the presence of liquid bridges. Powder Technology 114, 213-223.
Popov, V.L., 2010. Contact Mechanics and Friction-Physical Principles and Applications. Springer, Berlin.
Poutiainen, S., Matero, S., Hamalainen, T., Leskinen, J., Ketolainen, J., Jarvinen, K., 2012. Predicting granule size distribution of a fluidized bed spray granulation process by regime based PLS modeling of acoustic emission data. Powder Technology 228, 149-157.
Razzak, S.A., 2019. Flow characteristic studies on the gas-liquid-solid circulating fluidized bed based on system stability. International Journal of Multiphase Flow 113, 279-288.
Razzak, S.A., Barghi, S., Zhu, J.X., 2007. Electrical resistance tomography for flow characterization of a gas–liquid–solid three-phase circulating fluidized bed. Chemical Engineering Science 62, 7253-7263.
Sasic, S., Leckner, B., Johnsson, F., 2006. Time–frequency investigation of different modes of bubble flow in a gas–solid fluidized bed. Chemical Engineering Journal 121, 27-35.
Seville, J.P.K., Clift, R., 1984. The effect of thin liquid layers on fluidization characteristics. Powder Technology 37, 117-129.
Seville, J.P.K., Willett, C.D., Knight, P.C., 2000. Interparticle forces in fluidisation: a review. Powder Technology 113, 261-268.
Sun, J.Y., Wang, J.D., Yang, Y.R., 2012. CFD simulation and wavelet transform analysis of vortex and coherent structure in a gas-solid fluidized bed. Chemical Engineering Science 71, 507-519.
Sun, J.Y., Zhou, Y.F., Ren, C.J., Wang, J.D., Yang, Y.R., 2011. CFD simulation and experiments of dynamic parameters in gas-solid fluidized bed. Chemical Engineering Science 66, 4972-4982.
van der Schaaf, J., Schouten, J.C., Johnsson, F., van den Bleek, C.M., 2002. Non-intrusive determination of bubble and slug length scales in fluidized beds by decomposition of the power spectral density of pressure time series. International Journal of Multiphase Flow 28, 865-880.

van Ommen, J.R., Coppens, M.-O., van den Bleek, C.M., Schouten, J.C., 2000. Early warning of agglomeration in fluidized beds by attractor comparison. AIChE Journal 46, 2183-2197.
van Ommen, J.R., Sasic, S., van der Schaaf, J., Gheorghiu, S., Johnsson, F., Coppens, M.-O., 2011. Time-series analysis of pressure fluctuations in gas-solid fluidized beds - A review. International Journal of Multiphase Flow 37, 403-428.
van Ommen, J.R., van der Schaaf, J., Schouten, J.C., van Wachem, B.G., Coppens, M.-O., van den Bleek, C.M., 2004. Optimal placement of probes for dynamic pressure measurements in large-scale fluidized beds. Powder Technology 139, 264-276.
van Wachem, B.G.M., Schouten, J.C., Krishna, R., van den Bleek, C.M., 1998. Eulerian simulations of bubbling behaviour in gas-solid fluidised beds. Computers & Chemical Engineering 22, S299-S306.
van Wachem, B.G.M., Schouten, J.C., Krishna, R., van den Bleek, C.M., 1999. Validation of the Eulerian simulated dynamic behaviour of gas–solid fluidised beds. Chemical Engineering Science 54, 2141-2149.
van Willigen, F.K., van Ommen, J.R., van Turnhout, J., van den Bleek, C., 2003. Bubble size reduction in a fluidized bed by electric fields. International Journal of Chemical Reactor Engineering.
Wang, H.G., Dyakowski, T., Senior, P., Raghavan, R.S., Yang, W.Q., 2007. Modelling of batch fluidised bed drying of pharmaceutical granules. Chemical Engineering Science 62, 1524-1535.
Wang, T., He, Y., Tang, T., Peng, W., 2016. Experimental and numerical study on a bubbling fluidized bed with wet particles. Aiche Journal 62, 1970-1985.
Weigert, T., Ripperger, S., 1999. Calculation of the liquid bridge volume and bulk saturation from the half-filling angle. Particle & Particle Systems Characterization 16, 238-242.
Wen, C.Y., Yu, Y.H., 1966. Mechanics of fluidization. Chemical Engineering Progress Symposium Series 62, 100.
Wormsbecker, M., Pugsley, T., 2008. The influence of moisture on the fluidization behaviour of porous pharmaceutical granule. Chemical Engineering Science 63, 4063-4069.
Xu, H., Zhong, W., Yuan, Z., Yu, A., 2017. CFD-DEM study on cohesive particles in a spouted bed. Powder Technology 314, 377-386.
Yasui, G., Johanson, L., 1958. Characteristics of gas pockets in fluidized beds. AIChE Journal 4, 445-452.
Zhang, Y., Bi, H.T., Grace, J.R., Lu, C., 2010. Comparison of decoupling methods for analyzing pressure fluctuations in gas‐fluidized beds. AIChE Journal 56, 869-877.
Zhou, Y., Wang, J., Yang, Y., Wu, W., 2013a. Modeling of the temperature profile in an ethylene polymerization fluidized-bed reactor in condensed-mode operation. Industrial & Engineering Chemistry Research 52, 4455-4464.
Zhou, Y., Ren, C., Wang, J., Yang, Y., 2013b. Characterization on hydrodynamic behavior in liquid-containing gas-solid fluidized bed reactor. AIChE Journal 59, 1056-1065.
Zhou, Y., Shi, Q., Huang, Z., Liao, Z., Wang, J., Yang, Y., 2016a. Realization and control of multiple temperature zones in liquid-containing gas–solid fluidized bed reactor. AIChE Journal 62, 1454-1466.
Zhou, Y., Shi, Q., Huang, Z., Wang, J., Yang, Y., 2016b. Effects of liquid action mechanisms on hydrodynamics in liquid-containing gas–solid fluidized bed reactor. Chemical Engineering Journal 285, 121-127.
Zhou, Y., Shi, Q., Huang, Z., Wang, J., Yang, Y., 2017. Particle agglomeration and control of gas-solid fluidized

bed reactor with liquid bridge and solid bridge coupling actions. Chemical Engineering Journal 330, 840-851.
Zhu, J.X., Karamanev, D.G., Bassi, A.S., Zheng, Y., 2000. (Gas-)liquid-solid circulating fluidized beds and their potential applications to bioreactor engineering. The Canadian Journal of Chemical Engineering 78, 82-94.